Electronic Supplementary Material (ESI) for Physical Chemistry Chemical Physics.
This journal is © the Owner Societies 2023

Supplemental Material

Probe the Nanoparticle – Nucleus Interaction via Solvent Free Molecular Model

Liuyang Zhang [1] , Ning Liu [2*] and Xianqiao Wang [3]

1 State Key Laboratory for Manufacturing Systems Engineering, Xi'an Jiaotong University, Xi'an, Shaanxi 710049, People's Republic of China

2 School of Aerospace Engineering and Applied Mechanics, Tongji University, Shanghai 200092, P. R. China

3 College of Engineering, University of Georgia, Athens, GA 30602, USA

*Corresponding authors : 21019@tongji.edu.cn

1. Time unit derivation

The time unit τ is derived based on the diffusion coefficient *D*. As shown in Figure S1 (a), simulations have been performed on a square lipid bilayer membrane with the size 200 σ*200 σ to obtain diffusion coefficient *D*. The average mean squared displacement *MSD* of lipid beads have been collected and shown in Figure S1(b). Subsequently, the diffusion coefficient *D* could be calculated through the expression below [1],

$$MSD = \frac{1}{N}\sum_{i=1}^{N}[(x^i - {x_0}^i)^2 + (y^i - {y_0}^i)^2] = 4Dt \tag{S1}$$

in which x^i, y^i are the coordinate components of *i*th lipid bead at time *t* while ${x_0}^i$, ${y_0}^i$ are the initial coordinate components of *i*th lipid bead . The calculated diffusion coefficient is equal to 1×10^{-2} σ^2/τ, while the diffusion coefficient for lipids is around 5 $\mu m^2/s$ [2]. Therefore, the time unit τ is 2 ns.

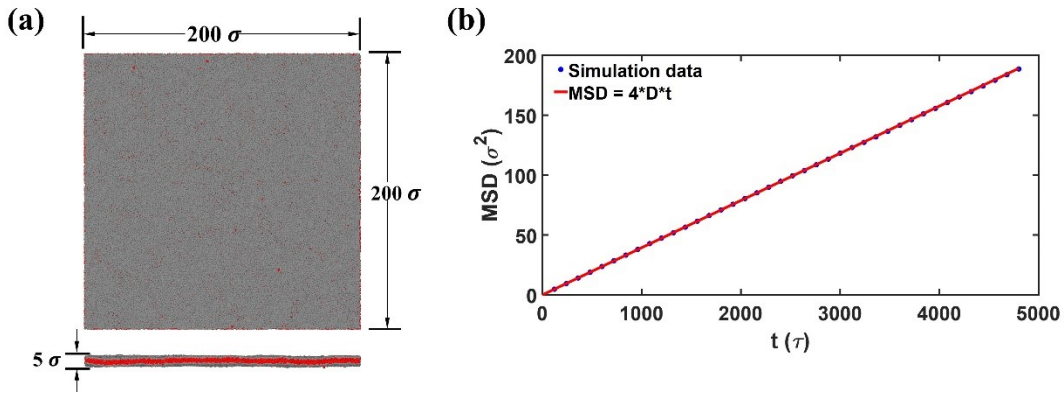

Figure S1. Diffusion tests for the lipid bilayer (a) overview of the simulation model (b) mean squared displacement of lipids.

2. Computational Method

2.1 Coarse-grained model of the nuclear membrane.

We applied Cooke and Deserno's solvent-free model of lipid bilayers based on an attractive potential.[3] This model can help reduce simulation time up to 90% as compared to a model with explicit solvents filling the entire simulation box. The following potentials are used in the simulation to describe the van der Waals interaction between beads:

The size of each lipid bead is fixed via a Weeks-Chandler-Andersen potential

$$U_{WCA} = 4\epsilon\left[\left(\frac{b}{r_{ij}}\right)^{12} - \left(\frac{b}{r_{ij}}\right)^{6} + \frac{1}{4}\right], r_{ij} < r_c = \sqrt[6]{2}b \quad \text{(S2)}$$

In order to ensure the cylindrical lipid shape, b is set as $b_{head,\,head} = b_{head,tail} = 0.95\sigma$ and $b_{tail,tail} = \sigma$. The three lipid beads are linked by two finite extensible nonlinear elastic FENE bonds

$$U_{FENE} = \sum_{bonds} -\frac{1}{2}k_b R_{max}^2 \ln\left(1 - \frac{r^2}{R_{max}^2}\right) \quad \text{(S3)}$$

with stiffness $k_b = 30\varepsilon/\sigma^2$ and divergence length $R_{max} = 1.5\sigma$. Lipids are straightened by a harmonic spring

$$U_{stretching} = \sum_{bonds} k_b(r - r_0)^2 \quad \text{(S4)}$$

with bending stiffness $k_b = 10\varepsilon/\sigma^2$ and equilibrium length 4σ between the head bead and the second tail bead. The absence of explicit solvents and the hydrophobic effect is compensated for by an attractive interaction between the tail beads. The potential we use to account for the hydrophobic effect is

$$U_{cos} = \begin{cases} -\varepsilon, & r < r_c \\ -\varepsilon cos^2[\pi(r - r_c)/2w], & r_c \le r \le r_c + w \\ 0, & r > r_c + w \end{cases} \quad \text{(S5)}$$

which describes an attractive potential with depth ε that smoothly tapers to zero for $r > r_c$. In our simulations, the decay range w is set as 1.6σ. The interaction between NPs and lipid heads in the nuclear pore and envelope is described by the Lennard-Jones potential function

$$U_{LJ} = 4\epsilon\left[\left(\frac{b}{r_{ij}}\right)^{12} - \left(\frac{b}{r_{ij}}\right)^{6}\right], r_{ij} < r_c = 2.5\sigma \quad \text{(S6)}$$

where r_{ij} is the distance between beads i and j. In the following,

Table S1. Interaction parameters for nuclear envelope, nuclear pore and NPs

Bead type	Bead type	Interaction Potential	Parameters
Lipid head (nuclear envelope and pore)	Lipid head (nuclear envelope and pore)	U_{WCA}	$b = 0.95\sigma$
Lipid head (nuclear envelope and pore)	Lipid tail (nuclear envelope and pore)	U_{WCA}	$b = 0.95\sigma$
Lipid tail (nuclear envelope and pore)	Lipid tail (nuclear envelope and pore)	U_{cos}	$b = \sigma, w = 1.6\sigma$
Lipid head (nuclear envelope and pore)	NPs	U_{LJ}	$b = \sigma$
Lipid tail (nuclear envelope and pore)	NPs	U_{WCA}	$b = 0.95\sigma$
NPs	NPs	U_{LJ}	$b = \sigma$

2.2 Coarse-grained model of elastic spherical NPs

A coarse-grained (CG) model [4-9], inspired by the concept of modelling red blood cells through CGMD simulations, was implemented to describe the interactions inside NPs

composed of thin shells of a triangular lattice spring network. Corresponding beads on the surface of NPs are evenly distributed, approximately 1σ between adjacent beads. Two adjacent beads would form one bond element, three adjacent beads would form one triangular element, while two triangular elements sharing one edge would form one bending element. The total potential energy of such an elastic NP can be expressed as

$$U_t = U_{bond} + U_{area} + U_{volume} + U_{bending}. \tag{S7}$$

The bond energy term U_{bond} represents in-plane stretching energy of the spring network expressed as

$$U_{bond} = \sum_{i=1}^{N_b} k_{bond}(l_i - l_i^0)^2 \tag{S8}$$

where N_b is the number of bonds, k_{bond} is the bond stiffness, l_i is the current length of the bond spring, and l_i^0 is the equilibrium length for *i*-th individual bond springs. The terms ε and σ are the basic units of energy and distance in our CGMD simulations, respectively. The bond potential used here is a variant of the harmonic bond potential which avoids significant residual stress in NPs due to its customized equilibrium length for each individual bond. The area potential can be expressed as

$$U_{area} = \frac{k_a(A_t - A_t^0)^2}{2A_t^0} + \sum_{i=1}^{N_a} \frac{k_d(A_i - A_i^0)^2}{2A_i^0}, \tag{S9}$$

where $k_a$and k_d are global and local area control coefficients for triangular elements, respectively. A_t and A_i are the current total surface area of the NP and the local area for *i*-th individual triangular element, respectively, while A_t^0 and A_i^0 are equilibrium total surface area of the NP and local surface area for *i*-th individual triangular element.

With parameters involved in those two energy terms, the in-plane stretching modulus of the elastic NP can be determined as [4],

$$K_s = k_a + k_d + \sqrt{3}k_{bond}. \tag{S10}$$

The volume energy term U_{volume} is expressed as:

$$U_{volume} = \frac{k_V(V - V^0)^2}{2V^0} \tag{S11}$$

where k_V is the global volume constraint coefficient of triangular elements. V and V^0 are the volume of the elastic NP and its equilibrium value, respectively.

The bending energy term $U_{bending}$ can be determined as:

$$U_{bending} = \sum_{i=1}^{N_{ob}} k_{bend}(1 - cos(\theta_i - \theta_i^0)) \tag{S12}$$

where N_{ob} is the number of bending elements, k_{bend} is the bending constant of bending elements, θ_i is the dihedral angle of the *i*-th bending element, and θ_i^0 is the equilibrium dihedral angle of the *i*-th individual bending element.

2. Effect of loading rate

To better understand the effect of the tensile loading rate on the mechanical properties of solvent free NPC model, we have performed supplementary simulation (Figure S2) to with same input parameters except for the tensile rate for the NPC model with diameter as $40\ \sigma$. It can be observed that the tensile rate plays an important role to mechanical stiffness of the NPC pore.

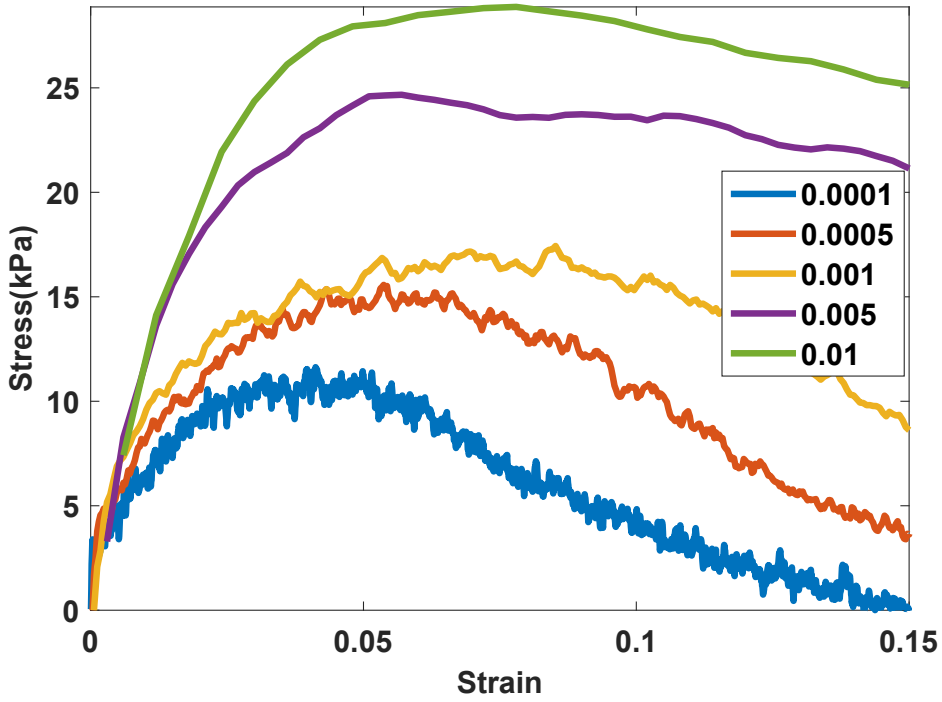

Figure S2. Strain-stress curve for nuclear pore with D_{pore} as $40\ \sigma$ under various tensile rate (unit $1/\tau$).

3. Morphological changes of nuclear pores during tension

As shown in Figure S3, the nuclear pores experience morphological changes from cylinder-like pores to the dumb-bell pores for nuclear pore complexes with different pore diameters D_{pore}. The dumb-bell pores have narrow necks due to the tension of the envelope plane.

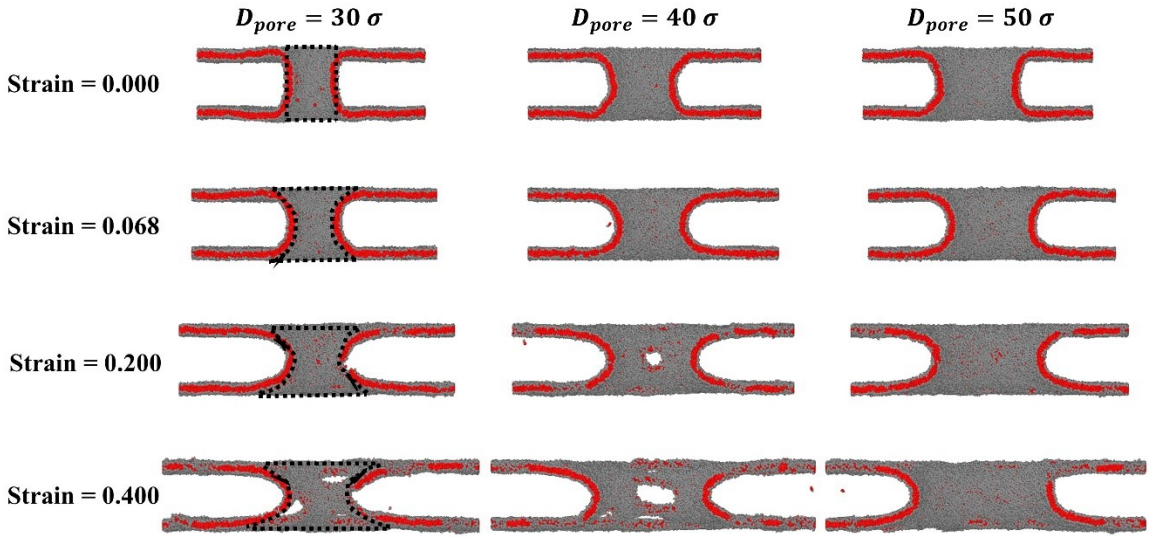

Figure S3. Morphological changes under biaxial stretch of the nuclear pores with different pore diameters D_{pore} .

3. Surface tension of solvent free NPC model

As noticed in snapshots embedded in Figure 2, beyond a critical stress or area per lipid, multiply damage spots can be nucleated and grow indefinitely to release the concentrated stress on the membrane plane. Lipid membrane stretching and damage opening is a critical factor to evaluate the structural stability of the solvent free NPC model. In order to quantitatively explain the damage generation on the nucleus biomembrane, the membrane tension is calculated and its evolution is examined (the bottom panel). The surface tension with a normal in the *z*-direction inside a nuclear membrane is characterized by the pressure tensor P using the following relation,[10]

$$\gamma = \int_{Z_1}^{Z_2} \left[P_N(Z) - P_T(Z)\right] dZ \tag{S13}$$

in which γ is the surface tension, P_N is the pressure normal to the bilayer membrane, and P_T is the tangential pressure along the bilayer surface. For particle simulations, this equation can be further simplified: [11]

$$\gamma = L_Z\left[P_Z - \left(P_X + P_Y\right)/2\right] \tag{S14}$$

In this equation (S14), L_Z is the size of simulation cell in the *z*-direction normal to the nuclear bilayer membrane and P_i is the pressure in the $i = x,y,z$ direction. The nuclear bilayer membrane is initially in an equilibrium tensionless state. Take the pore with size 30 σ for example (Figure S2), as the tension proceeds, multiply damage spots are nucleated on the nuclear membrane with the membrane tension up to $0.45\ pN/nm$, which agrees with the original solvent free model for the bilayer membrane.[3] The critical membrane tension required for damage spot nucleation under different NPC pore sizes indicates the inverse dependency of surface tension on the pore size; the larger the NPC pore on the nuclear membrane, the lower the critical surface tension required to damage spot nucleation. Previously, nanoscale stiffness topography analysis of the cytoplasmic side of the NPCs was performed using AFM nanoindentation, thus providing an estimate of the density of the NPC in the NE, the average indentation force and the stiffness of the

membrane. The average force data measured and the stiffness calculated was in the order of [pN*nm^{-1}].[12, 13] Results from our model in Figure S2 is in agreement with the magnitude order from the experimental measurements. Both measurements from Figure 2 and Figure S2 and relevant comparisons with experimental data lend reasonable credence to support that our solvent free model is reliable to capture the mechanical properties of the NPC and NE.

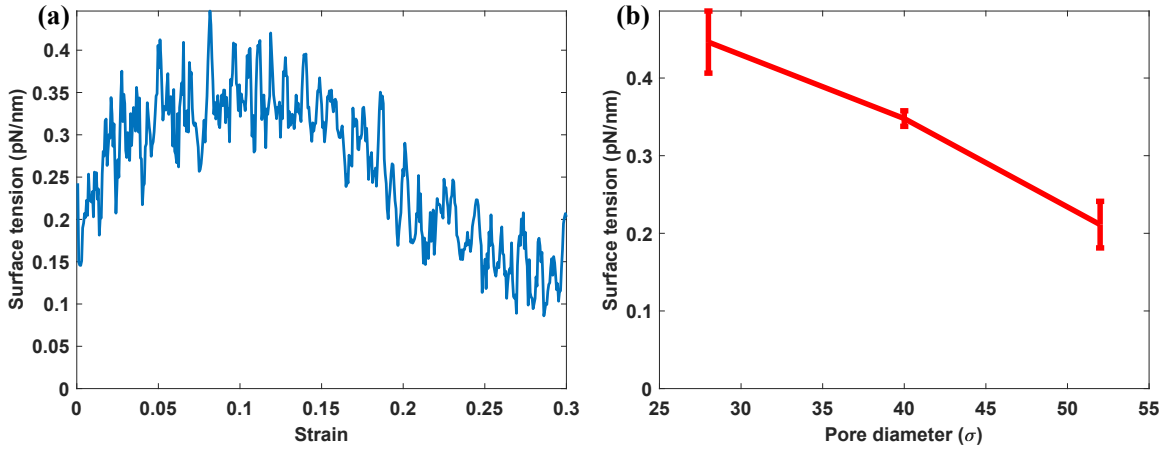

Figure S4. (a) The evolution of surface tension during the tensile process; (b) The maximum surface tension before the pore generation with regard to the pore size

4. Effect of surface modification on NP transport

In Figure 5, the dynamic NP transport process through the nuclear pore for different surface modification, namely $\epsilon = 0.4\ \varepsilon$ and $0.6\ \varepsilon$. It can be seen that the time spent for the full NP transport process increases as the interbead interaction strength ϵ increases. That could be attributed to the increasing nonlinear deformation of the nuclear pore complexes induced by the increasing interbead interaction strength ϵ, whuch holds the NP from detaching from the nuclear pore.

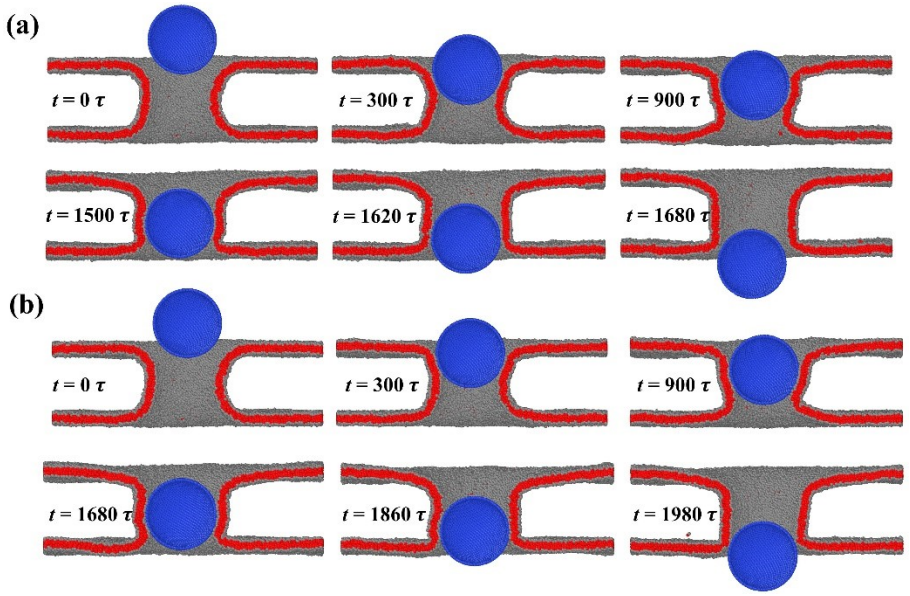

Figure S5. Effect of surface modification on dynamic NP transport process through the nuclear pore. (a) $\epsilon = 0.4\ \varepsilon$; (b) $\epsilon = 0.6\ \varepsilon$.

5. Effect of rigidity on spherical NP transport

As shown in Figure S6, the dynamic transport of elastic spherical NPs with different rigidity k_{np} have been shown. When the rigidity k_{np} is equal to 4, large deformation could be observed during the interaction between the NP and the nuclear pore complex as shown in Figure S6(a). As the rigidity k_{np} increases, the nuclear envelopes experience larger morphological changes while the shape of spherical NPs undergo marginal changes. Consequently, the time spent for the full NP transport process increases due to the enhanced shape adaptability as the rigidity k_{np} decreases.

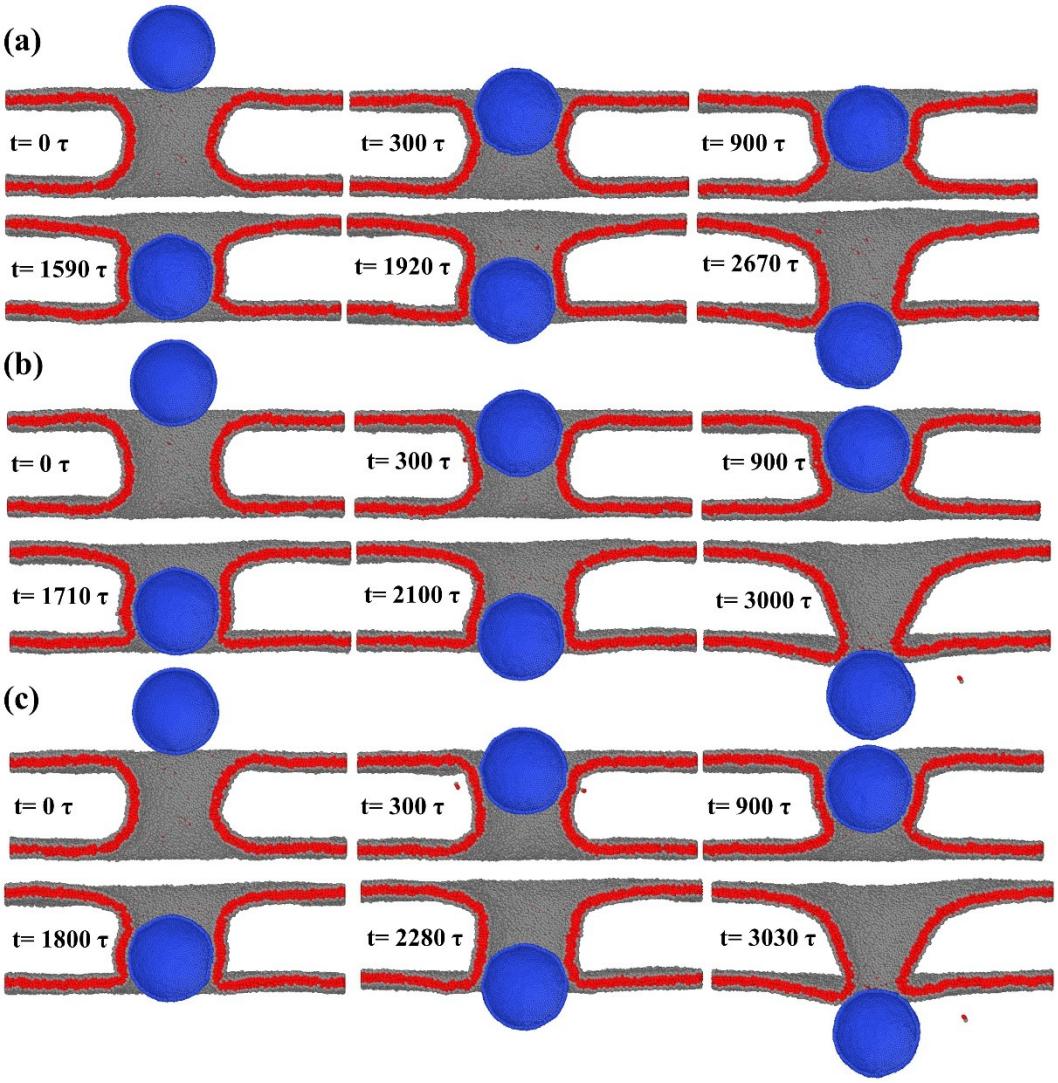

Figure S6 Dynamic elastic NP transport process through the nuclear pore by varying the rigidity as (a) $k_{np} = 2$; (b) $k_{np} = 4$, (c) $k_{np} = 10$ respectively.

6. Effect of rigidity on 2D NP transport

Here to unveil the transport process of elastic NP, two-dimensional NP ($100\,\sigma \times 16\,\sigma$) with 1910 hexagonally connected beads is selected as the intrabead bonds stiffness (k_{np}) are the only tunable mechanical parameter to obtain NP with various rigidities. For more details about the two-dimensional model, it can be referred to our previous studies of the characterization the NP. [14] As shown in Figure S7, the two-dimensional NP is horizontally placed $30\,\sigma$ away from the nuclear midplane and follows the same simulation setup as

previous implementations. When k_{np} is set to be $^{1}\ k_B T/\sigma^2$, the two-dimensal NP cannot maintain its two-dimensional features and pocesses large freedom of out-of-plane deformaiton. The soft NP exhibits kaleidoscopic morphologies to minimize the required passing energy. The softness of the two-dimensional NP allows itself to cater for the hyperbolic-like pore geometry and takes $4950\ \tau$ for the entire passage through the nuclear pore. When k_{np} is set to be $^{50}\ k_B T/\sigma^2$ that is same order of bond stiffness of membrane lipid, the NP can maintain its two-dimensional morphology when passing through the channel. It takes long time up to $2160\ \tau$ for the narrow end to approach the pore entrance as the two-dimensional NP with high length-width ratio had to piece into the nuclear pore via the narrow end. It is extremly time- and energy- consuming to pass through the channel from the wide end due to large deformation of the nuclear pore and comparable rigidity of the NP and nucleus. Due to large degree freedom of flexibility, the interaction between the flexible NP and nuclear pore is enhanced than that of rigid NP thus it takes longer time for the soft NP to pass through the nuclear pore.

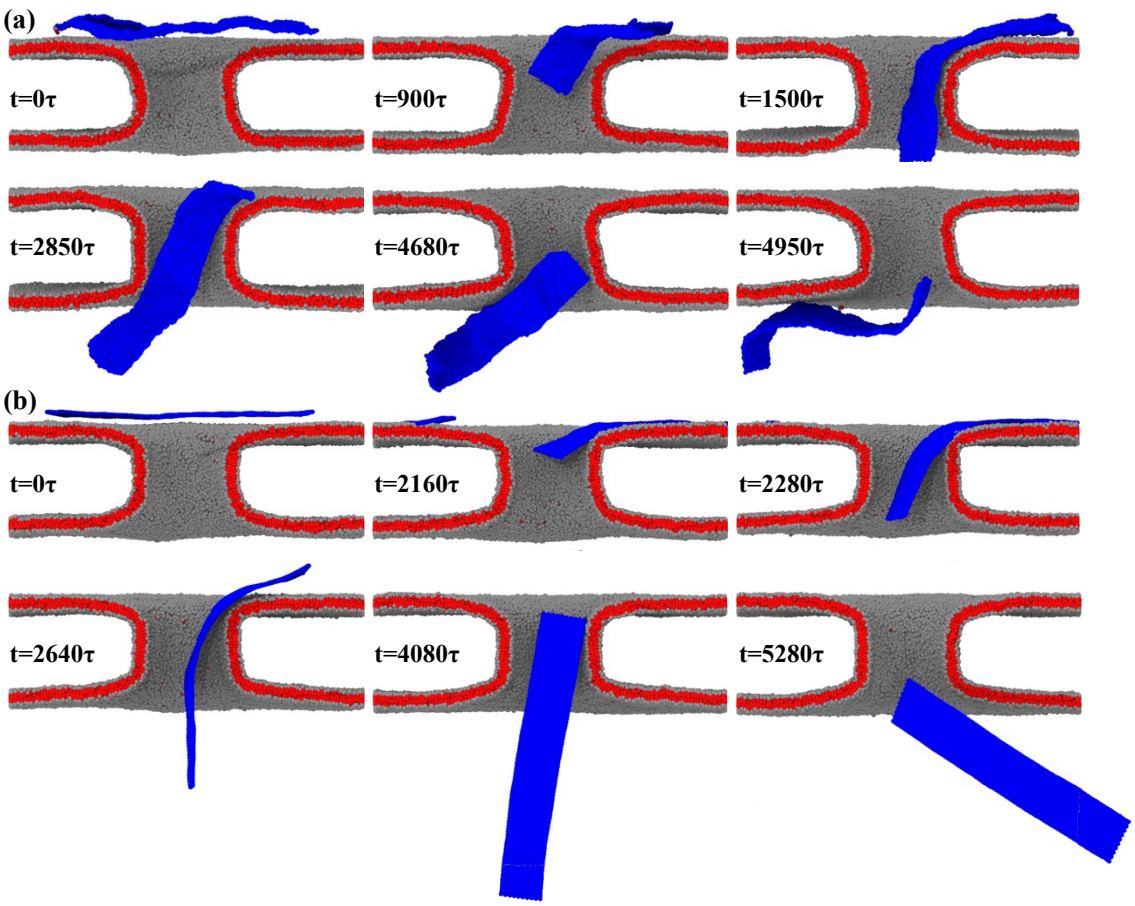

Figure S7. Dynamic two-dimensional NP transport process through the nuclear pore by varying the rigidity as (a) $k_{np} = 1\ k_B T/\sigma^2$; (b) $k_{np} = 50\ k_B T/\sigma^2$, respectively.

To unfold the effect of NP's flexibility on the transport process, NP's geometrical variations during the whole transport process are sampled by achieving the intrabead distance distribution among the NP beads in Figure S8(a). It can be seen that NP with $k_{np} = 1\ k_B T/\sigma^2$ exhibits smaller intrabead distance and more severe defromation than the NP with $k_{np} = 50\ k_B T/\sigma^2$ which indicates that NP's rigidities can regulate the transport pathway via the in-plane and out-of-plane deformation. The deformable NP is capable of entering into the nucleusplam through self-adjusting its morphology when passing through the nuclear pore with limited size. Similarly, the rigidity effect of NP on the transport process can be further verified by the free energy profile in Figure S8(b). The free energy required to pass through the nuclear pore for the soft NP is less than that consumed by the rigid two-dimensional NP. Different from previous studies about the interaction between

the soft NP and cell membrane,[15] it shows that rigid NPs require less energy for membrane internalization than that for soft NPs while the soft NPs must overcome a larger free energy barrier during the wrapping process by the cell membrane. By reproducing the transport process of two dimensional NP through nuclear pore, it indicates that the rigidity of the NP is another important factor that determines the exchange process between the cytoplasm and nucleusplam. Our findings might provide a meaningful strategy to design the mechanically tunable drug delivery vehicle to target the nucleus.

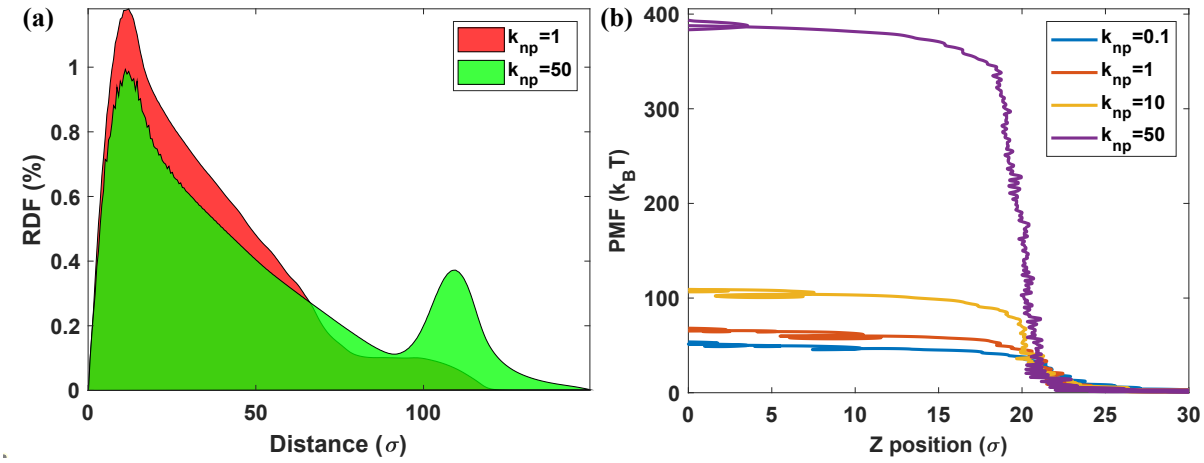

Figure S8. Evolution of intrabead distance (a) and free energy profile (b) during the transport process for NP with various rigidities of NP as $0.1\ k_BT/\sigma^2$, $1\ k_BT/\sigma^2$, $10\ k_BT/\sigma^2$ and $50\ k_BT/\sigma^2$

Reference

1. Cooke, I. R.; Deserno, M., Solvent-free model for self-assembling fluid bilayer membranes: Stabilization of the fluid phase based on broad attractive tail potentials. *The Journal of Chemical Physics* **2005,** *123* (22), 224710.
2. Orädd, G.; Lindblom, G.; Westerman, P. W., Lateral Diffusion of Cholesterol and Dimyristoylphosphatidylcholine in a Lipid Bilayer Measured by Pulsed Field Gradient NMR Spectroscopy. *Biophysical Journal* **2002,** *83* (5), 2702-2704.
3. Cooke, I. R.; Deserno, M., Solvent-free model for self-assembling fluid bilayer membranes: stabilization of the fluid phase based on broad attractive tail potentials. *J Chem Phys* **2005,** *123* (22), 224710.
4. Fedosov, D. A.; Caswell, B.; Karniadakis, G. E., A Multiscale Red Blood Cell Model with Accurate Mechanics, Rheology, and Dynamics. *Biophysical Journal* **2010,** *98* (10), 2215-2225.
5. Li, J.; Dao, M.; Lim, C. T.; Suresh, S., Spectrin-Level Modeling of the Cytoskeleton and Optical Tweezers Stretching of the Erythrocyte. *Biophysical Journal* **2005,** *88* (5), 3707-3719.

6. Shen, Z.; Ye, H.; Li, Y., Understanding receptor-mediated endocytosis of elastic nanoparticles through coarse grained molecular dynamic simulation. *Physical Chemistry Chemical Physics* **2018,** *20* (24), 16372-16385.
7. Shen, Z.; Ye, H.; Yi, X.; Li, Y., Membrane Wrapping Efficiency of Elastic Nanoparticles during Endocytosis: Size and Shape Matter. *ACS Nano* **2019,** *13* (1), 215-228.
8. Ye, H.; Shen, Z.; Li, Y., Computational modeling of magnetic particle margination within blood flow through LAMMPS. *Computational Mechanics* **2018,** *62* (3), 457-476.
9. Ye, H.; Shen, Z.; Yu, L.; Wei, M.; Li, Y., Anomalous Vascular Dynamics of Nanoworms within Blood Flow. *ACS Biomaterials Science & Engineering* **2018,** *4* (1), 66-77.
10. Simunovic, M.; Voth, G. A., Membrane tension controls the assembly of curvature-generating proteins. *Nat. Commun.* **2015,** *6*, 7219.
11. Chiu, S. W.; Clark, M.; Balaji, V.; Subramaniam, S.; Scott, H. L.; Jakobsson, E., Incorporation of surface tension into molecular dynamics simulation of an interface: a fluid phase lipid bilayer membrane. *Biophys. J.* **1995,** *69* (4), 1230-1245.
12. Garcia, A.; Rodriguez Matas, J. F.; Raimondi, M. T., Modeling of the mechano-chemical behaviour of the nuclear pore complex: current research and perspectives. *Integr Biol (Camb)* **2016,** *8* (10), 1011-1021.
13. Stanley, G. J.; Fassati, A.; Hoogenboom, B. W., Biomechanics of the transport barrier in the nuclear pore complex. *Seminars in Cell & Developmental Biology* **2017,** *68*, 42-51.
14. Zhang, L.; Xu, B.; Wang, X., Cholesterol Extraction from Cell Membrane by Graphene Nanosheets: A Computational Study. *The Journal of Physical Chemistry B* **2016,** *120* (5), 957-964.
15. Zhang, L.; Chen, H.; Xie, J.; Becton, M.; Wang, X., Interplay of Nanoparticle Rigidity and Its Translocation Ability through Cell Membrane. *The Journal of Physical Chemistry B* **2019,** *123* (42), 8923-8930.